

Feasibility of Non-Line-of-Sight Integrated Sensing and Communication at mmWave

Paolo Tosi^{*†}, Marcus Henninger^{*}, Lucas Giroto de Oliveira[‡], Silvio Mandelli^{*}

^{*}Nokia Bell Labs Stuttgart, Germany [†]Politecnico di Milano, Italy

[‡]Karlsruhe Institute of Technology (KIT), Germany

E-mail: marcus.henninger@nokia.com

Abstract—One rarely addressed direction in the context of Integrated Sensing and Communication (ISAC) is non-line-of-sight (NLOS) sensing, with the potential to enable use cases like intrusion detection and to increase the value that wireless networks can bring. However, ISAC networks impose challenges for sensing due to their communication-oriented design. For instance, time division duplex transmission creates spectral holes in time, resulting in spectral replicas in the radar image. To counteract this, we evaluate different channel state information processing strategies and discuss their tradeoffs. We further propose an ensemble of techniques to detect targets in NLOS conditions. Our approaches are validated with experiments using a millimeter wave ISAC proof of concept in a factory-like environment. The results show that target detection in NLOS is generally possible with ISAC.

Index Terms—6G, ISAC, NLOS Sensing, mmWave.

I. INTRODUCTION

One of the new features of upcoming sixth generation (6G) 3rd Generation Partnership Project (3GPP) cellular networks is the ability to gather information about the environment, essentially operating the network as a radar. The integration of this functionality into the existing cellular communications infrastructure is referred to as Integrated Sensing and Communication (ISAC). Recent research has been focusing, among other aspects, on the definition of plausible use cases for ISAC systems and their requirements [1], [2].

The typical assumption for most ISAC use cases is that targets are in line-of-sight (LOS) from transmitter (TX) and receiver (RX). However, radio signals may reach targets only indirectly via (multiple) reflections, e. g., off walls or buildings. Even though this would allow to acquire some information about the targets, non-line-of-sight (NLOS) sensing in ISAC is still a rather unexplored area of research. The main opportunity offered by NLOS sensing is the ability to enable use cases that are not possible with fixed camera or LiDAR systems, like “around-the-corner” detection. This feature would be particularly useful in applications such as safe urban mobility and surveillance systems for intrusion detection, where it is necessary to detect targets moving behind obstacles. In addition, the ability to operate in NLOS conditions would allow the

reuse of the same infrastructure deployed for communication purposes without the need for excessive densification.

Different NLOS sensing approaches using radar radios have been proposed in literature. For instance, target features such as breathing rate were extracted in NLOS conditions in [3] using frequency-modulated continuous-wave radar operating in millimeter wave (mmWave). In [4], micro-Doppler signatures of multiple human targets were extracted in a controlled urban scenario with an experimental coherent high-resolution X-band radar. A solution for performing NLOS detection of vehicles using a mmWave orthogonal frequency-division multiplexing (OFDM) radar was presented in [5], exploiting planar reflectors positioned at an L-shaped intersection. In a recent study, the authors of [6] used an experimental 60 GHz platform for human tracking in NLOS conditions indoors.

While the previous studies have shown promising results, they were performed using dedicated radar radios. However, the first envisioned cellular ISAC systems present substantially different challenges, since they are designed for communications and not yet optimized for sensing. For instance, they are bound to legacy frame structures and numerologies originally designed for communications. An example of this is the use of time division duplex (TDD), which creates spectral holes in time and requires dedicated channel state information (CSI) processing techniques to avoid undesired spectral replicas. This issue raises the distortion level in the radar image, impairing the feasibility of signal-to-noise ratio (SNR)-limited use cases, like NLOS sensing or drone detection.

To overcome this, we utilize CSI decimation to avoid spectral holes in time, thereby removing the replicas. We investigate the tradeoffs of different CSI processing techniques w. r. t. SNR and achievable sensing performance. Using different radar processing techniques to enable target detection, we leverage the resulting SNR and resolution gain to demonstrate the feasibility of intrusion detection based on ISAC in NLOS conditions. The experiments conducted with a mmWave ISAC proof of concept (POC) in an indoor environment show that target detection in NLOS is possible and indicate the fundamental feasibility of intrusion detection in ISAC.

II. ISAC SETUP

This work was developed using measurements from our ISAC POC [7], based on commercially available fifth generation (5G) communications hardware in frequency range 2

This work has been submitted to the IEEE for possible publication. Copyright may be transferred without notice, after which this version may no longer be accessible.

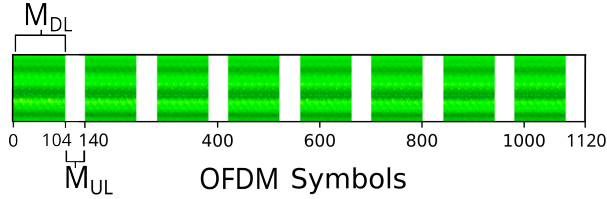


Fig. 1: CSI visualization of TDD pattern of one frame. Green columns represent DL symbols, blank columns correspond to UL symbols.

(FR2) at central frequency $f_c = 27.4$ GHz. The system comprises a half-duplex gNodeB (gNB) radio unit (RU) acting as TX, extended by a sniffer RU serving as RX. The RUs are physically separated, but quasi co-located, allowing to treat the system as a mono-static sensing setup. The gNB RU transmits 5G compliant OFDM radio frames with $T_f = 10$ ms duration in TDD. Each TDD pattern extends over $T_{\text{TDD}} = 1.25$ ms [8] and comprises $M_{\text{DL}} = 104$ downlink (DL) and $M_{\text{UL}} = 36$ uplink (UL) symbols, i. e., a DL/UL ratio of ca. 3:1. The sniffer RU is synchronized with the gNB RU and it always operates in UL. A dedicated server receives the transmitted and received signals as complex IQ samples from gNB RU and sniffer RU, respectively, and computes the CSI matrix $\mathbf{H} \in \mathbb{C}^{N \times M}$ via division of the reflected signal by the transmitted signal per frame. Moreover, gNB RU and sniffer RU use the same fixed beam (with 14° half-power horizontal beam width) for transmitting the signal and receiving the reflections, respectively. The POC parameters based on numerology $\mu = 3$ [9] are listed in Tab. I. For more details, please refer to [7].

The achievable system performance can be evaluated in terms of resolution and unambiguous aperture for both range and speed. Unambiguous range d_{unamb} and speed v_{unamb} are the maximum values without ambiguities due to aliasing, and depend on the sampling rate in frequency and time domain, defined by the subcarrier spacing Δf and the OFDM symbol time T_s , respectively. Range and speed resolution, d_{res} and v_{res} , refer to the ability to discriminate targets based on their range and speed. The resolution depends on the aperture in frequency and time, given by the bandwidth $N\Delta f$ and observation time MT_s , respectively [10]. Computing the periodogram [11] by processing the CSI of a single frame with the parameters from

TABLE I. POC SYSTEM PARAMETERS.

Parameter	Description	Value
f_c	Carrier frequency	27.4 GHz
B	Total bandwidth $N \cdot \Delta f$	190 MHz
N	Number of subcarriers	1584
M	Number of OFDM symbols per radio frame	1120
Δf	Subcarrier spacing	120 kHz
T_0	OFDM symbol time	8.33 μ s
T_{CP}	CP length	0.59 μ s
T_s	OFDM symbol time including CP	8.92 μ s

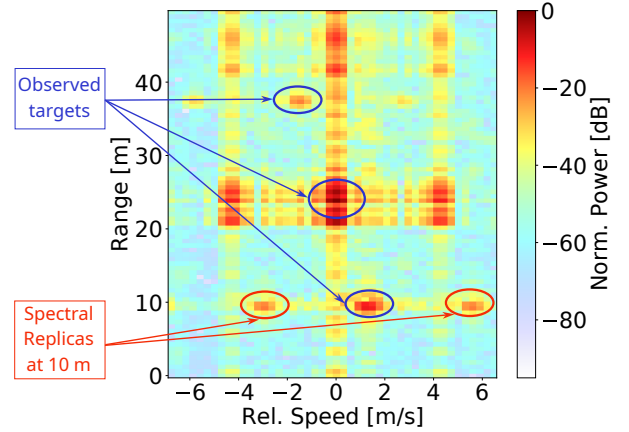


Fig. 2: Periodogram after processing a full single CSI matrix. Target returns are highlighted in blue, spectral replicas due to empty UL symbols for a target at 10 m highlighted in red.

Tab. I, the POC operates with the following performance

$$v_{\text{unamb}} = \frac{c_0}{2f_c T_s} = 613.5 \text{ m/s}, \quad (1)$$

$$d_{\text{unamb}} = \frac{c_0}{2\Delta f} = 1250 \text{ m}, \quad (2)$$

$$v_{\text{res}} = \frac{c_0}{2T_s f_c M} = 0.55 \text{ m/s}, \quad (3)$$

$$d_{\text{res}} = \frac{c_0}{2\Delta f N} = 0.79 \text{ m}. \quad (4)$$

Another important parameter is the SNR in the periodogram, which we define as the ratio between the strongest return in the periodogram and the measured noise level in the periodogram

$$\text{SNR} = \frac{\max(S(n, m))}{\sigma_N^2}. \quad (5)$$

The periodogram SNR includes a multiplicative processing gain given by the number of subcarriers and OFDM symbols. Thus, to maximize this gain, one would like to use the full CSI matrix \mathbf{H} for sensing. A high SNR is essential to distinguish targets from noise and especially critical for NLOS sensing, where the received reflected signal power is typically low due to the propagation distance and multiple reflections.

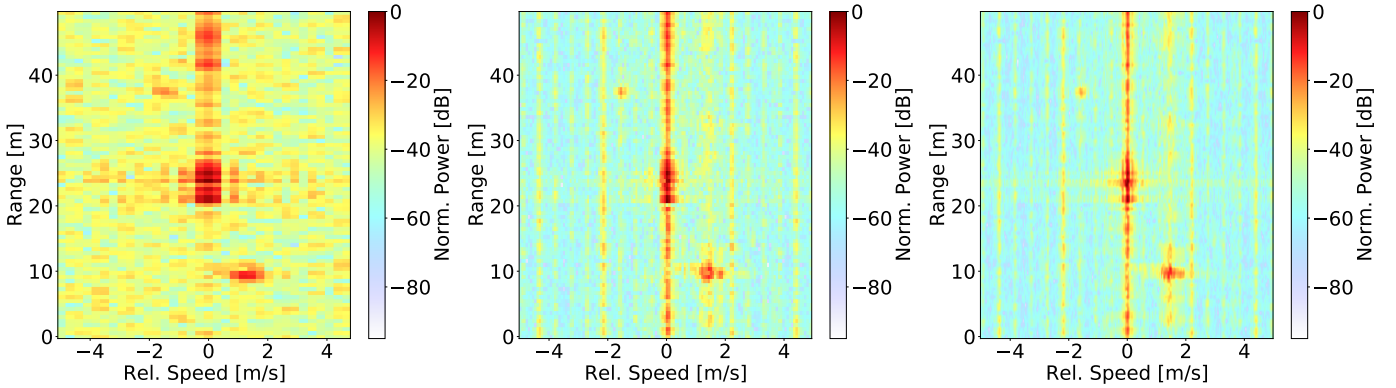
III. TIME DIVISION DUPLEX IN ISAC

A. Impact of Time Domain Holes

After obtaining \mathbf{H} , the range/Doppler periodogram is obtained by computing a DFT over the OFDM symbols and an IDFT over the subcarriers [11]

$$S(n, m) = \frac{1}{N'M'} \left| \sum_{k=0}^{N'} \left(\sum_{l=0}^{M'} \mathbf{H}(k, l) e^{-j2\pi \frac{lm}{M'}} \right) e^{j2\pi \frac{kn}{N'}} \right|^2, \quad (6)$$

where $N' = 2^{\lceil \log_2 N \rceil}$ and $M' = 2^{\lceil \log_2 M \rceil}$ are the number of rows and columns of \mathbf{H} after zero padding. Note that sidelobes in the periodogram can be controlled by element-wise multiplication of \mathbf{H} with a 2D window function. In our experiments, Chebyshev windowing was used.



(a) Periodogram with single frame, decimated to 24 symbols ($J = 47$). (b) Periodogram with 6 frames, decimated to 16 symbols per frame ($J = 70$) and concatenated. (c) Periodogram with 10 frames, decimated to 16 symbols per frame ($J = 70$) and concatenated.

Fig. 3: Examples of possible decimation and combining approaches for periodogram processing.

In standard sensing operations, we process the whole CSI matrix \mathbf{H} corresponding to each frame to maximize the processing gain and to achieve the speed resolution as in Eq. (3). However, since the gNB transmits in a TDD pattern, UL symbols do not contain useful information for radar processing and are discarded (set to zero) before computing the periodogram. Using TDD, each UL/DL pattern is repeated $T_f/T_{\text{TDD}} = R$ times per frame. With the parameters from Section II, this amounts to $R = 8$ TDD patterns, as shown in Fig. 1. Setting the UL parts to zero acts as an additional windowing effect on \mathbf{H} and introduces spectral replicas in the speed domain, as shown in Fig. 2. This “on/off” windowing is described by a discrete rectangle function (Dirichlet window) convolved with a train of Dirac deltas in the time domain

$$w_{\text{TDD}}(k) = \text{rect}\left(\frac{k + M_{\text{UL}}/2}{M_{\text{DL}} \cdot T_s}\right) * \sum_{i=0}^7 \delta(k - i \cdot T_{\text{TDD}}). \quad (7)$$

Its Fourier transform is a cardinal sine (Dirichlet Kernel) function multiplied by a train of Dirac deltas, which is convolved with the target in the speed (Doppler) domain. Therefore, after windowing and computing the periodogram, each target experiences replicas spaced by $R \cdot v_{\text{res}} = 4.4$ m/s in speed due to the frequency of the windowing in time.

B. CSI Processing Techniques

Processing only the first DL sequence with $M_{\text{DL}} = 104$ symbols would avoid replicas. However, per Eq. (3), this reduces the speed resolution to 5.88 m/s, which is unacceptable for most use cases.

Alternatively, the CSI matrix can be downsampled in time by selecting only every J -th OFDM symbol to avoid UL parts. This approach is effective in removing the replicas but reduces the unambiguous speed due to the decimation factor J . Further, the processing gain is decreased due to the reduced number of processed symbols, leading to a lower SNR.

• *Single frame processing.* By processing a single frame, it is possible to sample one symbol every J , thus with index m , where $\text{mod}(m, J) = 0$. For instance, $J = 47$ allows

selecting 3 symbols for every DL sequence and skipping the UL symbols completely. Fig. 3a shows an exemplary periodogram with this approach. As the number of symbols is reduced from 1120 to 24, an SNR loss is visible compared to Fig. 2. As presented in Tab. II, this amounts to a measured loss of 15.7 dB in the periodogram, in line with the expected $10 \log_{10}(1120/24) = 16.7$ dB. This loss can usually not be tolerated in NLOS scenarios, since the target return is typically weak due to the signal experiencing multiple reflections. With $J = 47$, the unambiguous speed is reduced to 13.05 m/s, which is still acceptable for most indoor use cases.

• *Multiple frame processing.* To increase the processing gain, consecutive frames can be concatenated after decimating, increasing both the number of processed symbols and the time aperture of the acquisition. However, with $J = 47$, only a single frame can be decimated before selecting UL symbols. By increasing the decimation to $J = 70$, it is possible to select 2 symbols from every DL section, with uniform rate over an indefinite number of frames without sampling UL symbols. This allows to compute the periodogram from K consecutive frames concatenated together. The resulting unambiguous speed of 8.76 m/s is still enough for most indoor use cases. As can be seen in Figs. 3b and Figs. 3c, this approach offers an increased SNR in the periodogram and a better speed resolution due to the increased time aperture. However, this comes at the cost of higher resource requirements and a lowered update rate. Compared to tracking and positioning tasks, in intrusion detection use cases a lowered update rate is less critical than a low SNR. However, it is possible, to retain a sufficiently large number of updates by letting consecutive observation windows overlap and setting an observation window stride $V < K$. Further, it should be noted that a large time aperture can lead

TABLE II. PERIODOGRAM SNR FOR DIFFERENT SETUPS.

Frames K	Decimation J	Symbols M	SNR [dB]
1	1	1120	60.91
1	47	24	45.16
6	70	96	52.35
10	70	160	54.66

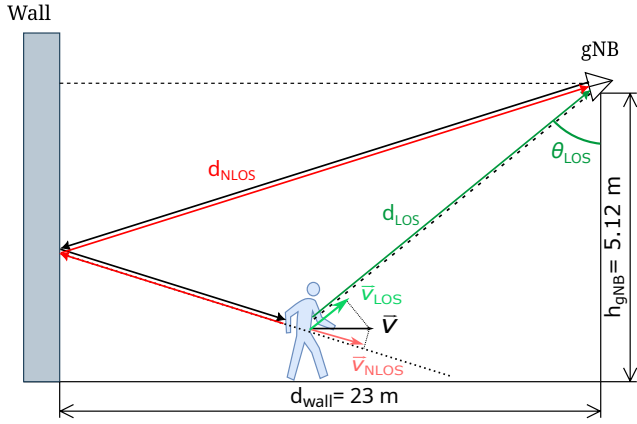


Fig. 4: Geometry of the measurement scenario. The target moves back and forth in a straight line between the wall and the gNB.

to target migration effects, caused by the target's range and speed varying within the observation window.

IV. NLOS EXPERIMENTS

A. NLOS Scenario

The two RUs of the ISAC POC are mounted at a height of $h_{\text{gNB}} = 5.12$ m and oriented towards a wide investigation area in the ARENA2036 industrial research campus in Stuttgart, Germany. The antenna pole is located at a horizontal distance of approximately $d_{\text{wall}} = 23$ m from a warehouse rack (installed in front of a concrete wall) and a cargo door. The measurement area is free of major obstructions that could be used to create a NLOS scenario under normal conditions. However, it is possible to emulate NLOS conditions by directing the signal over the target towards the wall and observing the reflected returns, as shown in Fig. 4. Further, due to the large beamwidth, both LOS and NLOS returns are present in our measurements. In our study, the LOS component is used as a source of ground truth as a rough estimate of the target position. However, LOS information has no bearing on the NLOS detection capabilities of our setup, but it is merely used as a simple remedy in the absence of accurate ground truth.

The scope of the experiments with the described setup was to determine the presence of the target via the NLOS return. At each update, given the geometry of the measurement described in Fig. 4, the expected speed and range of the NLOS target return is estimated from the LOS component as

$$\hat{v}_{\text{NLOS}} \approx -v_{\text{LOS}}, \quad (8)$$

$$\hat{d}_{\text{NLOS}} = 2d_{\text{wall}} - d_{\text{LOS}} \cdot \sin(\theta_{\text{LOS}}), \quad (9)$$

where $\theta_{\text{LOS}} = \arccos(h_{\text{gNB}}/d_{\text{LOS}})$. Peaks in the NLOS region are compared with the expected target position, allowing to determine whether they correspond to the return generated by the target or to interference. If the NLOS range and speed match those estimated from ground truth, detection is positive. The detection rate is computed as the ratio of frames in which the NLOS component was detected to the total number of frames in which the LOS component was present.

B. Radar Detection

After obtaining the periodogram with Eq. (6), it must be determined whether bins contain returns corresponding to targets of interest. For this purpose, statistical tests are available in literature to decide whether a peak is due to noise only, or noise plus echos coming from a target. The detection test used in this work belongs to the family of constant false alarm rate (CFAR) detectors [12]. Based on the observed interference level and a pre-defined probability of false alarm p_{FA} , standard CFAR defines a threshold for the whole periodogram as

$$\eta_{\text{CFAR}} = -\sigma_N^2 \ln\left(1 - (1 - p_{\text{FA}})^{\frac{1}{NM}}\right). \quad (10)$$

In this work, we use a range-adjusted exponential threshold [13], which is set by combining Eq. (10) with an $1/d^2$ -shaped threshold to account for the propagation loss of target returns, which is proportional to the square of the distance to the RX. The threshold for a bin corresponding to range d is

$$\eta_{\text{exp}} = \eta_{\text{CFAR}} + \frac{\alpha}{d^2}, \quad (11)$$

where α is an adjustment factor for the exponential term. For this particular implementation, it is defined as the square root of the maximum return in the periodogram. The presence of a target is decided by comparing the signal level in every periodogram bin with this threshold.

C. Clutter Removal

A known problem in radar is created by unwanted returns generated by objects in the environment, that are not of interest for the radar scope, and generally referred to as clutter. In this work, clutter components are removed from the CSI matrix using subspace-based methods as described in [14]. The clutter removal matrices are obtained from calibration measurements with few acquisitions without targets. Data obtained from the clutter acquisition step can also be radar-processed, extracting information about the environment without targets, such as the distance of the wall/cargo gate in Fig. 4.

D. NLOS Processing

LOS sensing capabilities of our system have been demonstrated in [7]. The focus is now on whether it is possible to monitor areas in NLOS to enable intrusion detection services with ISAC. For this, the returns in the periodogram generated by targets in NLOS conditions must be determined. To ensure NLOS coverage, the signal must be directed towards a large obstacle with a sufficient radar cross-section before being reflected towards the target, similar to Fig. 4. Any return with a range greater than the wall can then be considered a NLOS return. However, distinguishing static targets from clutter can be challenging, as static clutter is generated by other multipath reflections. For NLOS intrusion detection, it is sufficient to detect an intruder only when it moves. Therefore, bins of the periodogram corresponding to null speed are discarded for NLOS processing. After extracting the position of the wall during calibration, the periodograms processed during online sensing operations are divided into two regions, corresponding

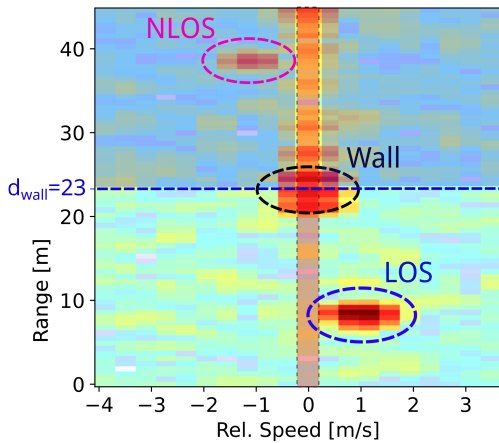


Fig. 5: Exemplary periodogram from the scenario presented in Sec. IV-A. The static return at d_{wall} is generated by the wall, and the joint LOS-NLOS returns from the moving target are highlighted. The NLOS region is highlighted in blue, discarded static bins in red.

to LOS and NLOS conditions, respectively. Fig. 5 highlights the separation for a sample periodogram, where the return from the moving target at ca. 40 m is considered NLOS.

V. MEASUREMENT RESULTS

We tested the NLOS detection capabilities on human targets, moving in the emulated NLOS environment between wall and gNB (Fig. 4). The results were obtained by concatenating multiple frames after decimating the CSI as presented in Sec. III. After computing the periodogram, targets were detected using the range-adjusted exponential threshold from Eq. (11).

The detection rate was estimated for the 10 strongest NLOS returns, comparing them with the LOS components. With the focus on intrusion detection, it is sufficient to detect the presence of the intruder once and raise an alarm accordingly. A possible approach for discriminating the presence of actual targets from false alarms is to verify that NLOS peaks are continuously detected within a window of consecutive updates. In our measurements, an overall detection rate of up to 67% was obtained with $K = 8$ frames and stride $V = 2$ frames.

The sustained presence of the NLOS return over an observation window can be evaluated by computing the moving average of the detection rate over time. Fig. 6 depicts the detection rate over a 0.5 s time window across the measured scenario. The calculation of the detection rate includes the parts of the measurements where the target stopped and changed direction (highlighted in red in Fig. 6). In these instances, no NLOS component is detected, as the bins of the periodogram corresponding to zero speed are discarded as described in IV-D. It can be observed that the NLOS component is detected in a sustained way when the target is moving, allowing reliable detection with further processing.

VI. CONCLUSION

In this work, we investigated NLOS sensing for ISAC. Based on measurements with a mmWave POC in a factory-like environment, we showed that target detection in NLOS is generally possible, enabling promising use cases like intrusion

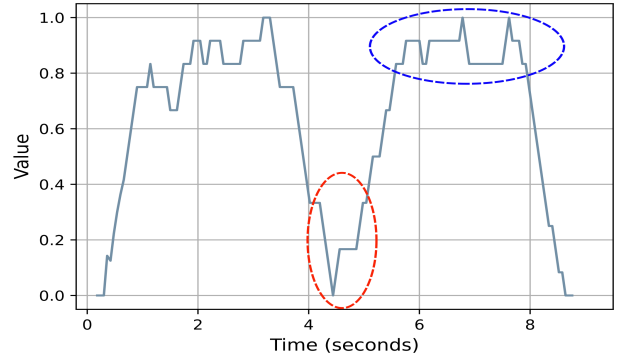


Fig. 6: Moving average of NLOS detections over a 0.5 s time window, using exponential threshold and clutter removal. Periodograms were generated using CSI matrices from $K = 8$ frames.

detection. To achieve that, we designed a CSI processing and detection routine that allows coping with the specifics of communications systems, while attaining the necessary SNR and resolution to detect moving objects in NLOS.

In the future, we will refine the detection routine, integrating also tracking techniques to further increase the reliability of the approach. Moreover, we plan to validate our method with additional measurements in other scenarios.

ACKNOWLEDGMENTS

The authors would like to thank Artjom Grudnitsky for the fruitful discussions during the development of this work and for his help in taking the measurements.

This work was developed within the KOMSENS-6G project, partly funded by the German Ministry of Education and Research under grant 16KISK112K.

REFERENCES

- [1] S. Mandelli, M. Henninger, M. Bauhofer, and T. Wild, "Survey on Integrated Sensing and Communication Performance Modeling and Use Cases Feasibility," in *2023 2nd Int. Conf. on 6G Netw.*, Oct. 2023.
- [2] J. Wang, N. Varshney, C. Gentile, S. Blandino, J. Chuang, and N. Golmie, "Integrated Sensing and Communication: Enabling Techniques, Applications, Tools and Data Sets, Standardization, and Future Directions," *IEEE Internet of Things J.*, vol. 9, no. 23, p. 23416–23440, Dec. 2022.
- [3] G. Li, Y. Ge, Y. Wang, Q. Chen, and G. Wang, "Detection of Human Breathing in Non-Line-of-Sight Region by Using mmWave FMCW Radar," *IEEE Trans. on Instrum. and Meas.*, vol. 71, p. 1–11, Sep. 2022.
- [4] M. Gustafsson, A. Andersson, T. Johansson, S. Nilsson, A. Sume, and A. Örbom, "Extraction of Human Micro-Doppler Signature in an Urban Environment Using a "Sensing-Behind-the-Corner" Radar," *IEEE Geosci. and Remote Sens. Lett.*, vol. 13, no. 2, p. 187–191, Feb. 2016.
- [5] D. Solomitskii, C. B. Barneto, M. Turunen, M. Allén, Y. Koucheryavy, and M. Valkama, "Millimeter-Wave Automotive Radar Scheme With Passive Reflector for Blind Corner Conditions," in *2020 14th Eur. Conf. on Antennas and Propag.*, 2020, pp. 1–5.
- [6] J. Pegoraro *et al.*, "JUMP: Joint communication and sensing with Unsynchronized transceivers Made Practical," *IEEE Transactions on Wireless Communications*, 12 2024.
- [7] T. Wild, A. Grudnitsky, S. Mandelli, M. Henninger, J. Guan, and F. Schaich, "6G Integrated Sensing and Communication: From Vision to Realization," in *2023 20th Eur. Radar Conf.*, Sep. 2023, pp. 355–358.
- [8] 3GPP, "NR; Radio Resource Control (RRC); Protocol specification," Technical Specification (TS) 38.331, (2023), version 17.5.0.

- [9] —, “NR; Physical channels and modulation,” Technical Specification (TS) 38.211, 2023, version 17.4.0.
- [10] L. Giroto de Oliveira, B. Nuss, M. B. Alabd, A. Diewald, M. Pauli, and T. Zwick, “Joint radar-communication systems: Modulation schemes and system design,” *IEEE Trans. on Microwave Theory and Techn.*
- [11] K. M. Braun, “OFDM Radar Algorithms in Mobile Communication Networks,” Ph.D. dissertation, Karlsruher Institut für Technologie, 2014.
- [12] M. A. Richards, J. A. Scheer, and W. A. Holm, *Principles of Modern Radar: Basic Principles*. Raleigh, NC, USA: SciTech Pub., 2010.
- [13] T. Wagner, R. Feger, and A. Stelzer, “Radar Signal Processing for Jointly Estimating Tracks and Micro-Doppler Signatures,” *IEEE Access*, vol. 5, p. 1220–1238, Feb. 2017.
- [14] M. Henninger, S. Mandelli, A. Grudnitsky, T. Wild, and S. ten Brink, “CRAP: Clutter Removal with Acquisitions Under Phase Noise,” in *2023 2nd Int. Conf. on 6G Networking*, Oct. 2023.